Ultraviolet suppression and nonlocality in optical model potentials for nucleon-nucleus scattering

H. F. Arellano[1] and G. Blanchon[2,3]

[1] Department of Physics - FCFM, University of Chile, Av. Blanco Encalada 2008, Santiago, Chile
[2] CEA,DAM,DIF, F-91297 Arpajon, France
[3] Université Paris-Saclay, CEA, Laboratoire Matière en Conditions Extrêmes,Bruyères-le-Châtel, France

Abstract. We investigate the role of high momentum components of optical model potentials for nucleon-nucleus scattering and its incidence on their nonlocal structure in coordinate space. The study covers closed-shell nuclei with mass number in the range $4 \le A \le 208$, for nucleon energies from tens of MeV up to 1 GeV. To this purpose microscopic optical potentials are calculated using density-dependent off-shell g matrices in Brueckner-Hartree-Fock approximation and based on Argonne v_{18} as well as chiral $2N$ force up to next-to-next-to-next-to-leading order. We confirm that the gradual suppression of high-momentum contributions of the optical potential results in quite different coordinate-space counterparts, all of them accounting for the same scattering observables. We infer a minimum cutoff momentum Q, function of the target mass number and energy of the process, that filters out irrelevant ultraviolet components of the potential. We find that when ultraviolet suppression is applied to Perey-Buck nonlocal potential or local Woods-Saxon potentials, they also result nonlocal with similar appearance to those obtained from microscopic models in momentum space. We examine the transversal nonlocality, quantity that makes comparable the intrinsic nonlocality of any potential regardless of its representation. We conclude that meaningful comparisons of nonlocal features of alternative potentials require the suppression of their ultraviolet components.

PACS. 24.10.Ht Optical models (nuclear reactions) – 03.65.Nk Nonrelativistic theory of scattering – 25.40.Cm, 25.40.Dn Nucleon-induced reactions – 24.10.Cn Many-body theory in nuclear reaction models

1 Introduction

It is a broadly accepted fact that optical model potentials for nucleon-nucleus (NA) scattering are energy-dependent, complex and nonlocal operators. Their nonlocality arises from the fermionic nature of the interacting nucleons in conjunction with intrinsic nonlocalities of nucleon-nucleon (NN) interactions. By locality it is alluded to a particular structure of the interaction in coordinate space, being diagonal in the pre- and post-collision relative coordinates. An early departure from this construction was introduced by Perey and Buck (PB) in the early 60s [1], with the inclusion of a phenomenological finite-width Gaussian form factor in the central part of the potential. The width of the Gaussian is customary used to quantify the degree of nonlocality, being still broadly used [2,3,4,5].

In a recent work [6] we have investigated the nonlocal structure of microscopic folding optical-model potentials calculated in momentum space. The study focuses on proton scattering off ^{40}Ca at energies from 30 MeV up to 1 GeV. An important result of that investigation is that scattering observables and associated wavefunctions remain invariant under the suppression of momentum components of the potential above some cutoff momentum Λ.

Interestingly, the implied potentials in coordinate space exhibit quite different nonlocal structure. In this work we elaborate further those finding by considering targets over the mass range $4 \le A \le 208$. We find that the suppression of high momentum components of any potential leads to equivalent ones with comparable shape in coordinate space.

Historically, the construction and calculation of optical model potentials has adopted routes spanning from pure phenomenological models to strictly microscopic ones. Additionally, they can either be developed in coordinate or momentum representations. Furthermore, within the coordinate-space class, they can also be subdivided into local and nonlocal ones. On each of these approaches there are particular features of the potential which are often scrutinized such as depth, radii, diffuseness, nonlocality, and off-shellness, to mention some of the most common. Comparisons among these models can be made only at the end point, after solving Schrödinger equation, assessing their scattering amplitudes and level of agreement with scattering measurements.

Woods-Saxon potentials constitute a classic example of phenomenological local potential in coordinate space. In the model, various parameters are adjusted in order

to account for scattering data. In this work we pay attention to the global optical model potential by Koning-Delaroche [7], developed for nucleon energies of up to 200 MeV. The inclusion of nonlocality introduced by Perey-Buck folds a nonlocal form factor in the central part of the potential. The nonlocality is controlled through the width β of a Gaussian form factor, typically of the order of 0.8 fm. A recent parametrization of PB model has been introduced by Tian-Pang-Na [8] (TPM), enabling proton scattering for nucleon beam energies of up to 30 MeV.

Microscopic optical potentials have the interesting feature that provide a link between the bare NN interaction and the $(A+1)$-body system. Pioneering work along this line was introduced by Brieva and Rook [9], with the first microscopic folding approach for NA scattering. Simultaneously Jeukenne, Leujene and Mahaux [10], introduce the local density approximation for the optical model potential. Here, at each coordinate r of the projectile in the nucleus, the on-shell mass operator from infinite nuclear matter –evaluated at the density of the target at coordinate r– is mapped to the local potential. The energy at which the mass operator is evaluated corresponds to that of the beam.

Motivated from these advances, local NN effective interactions were developed by von Geramb [11] and subsequently by Amos and collaborators [12], to be used in the calculation of microscopic nonlocal optical potentials in coordinate space. The resulting strengths of Yukawa form factors of Hamburg and Melbourne NN effective interactions have been embedded in the DWBA98 computational code developed by Jacques Raynal [13], where the nonlocal part of the potential arises from the exchange term of the interaction. Applications of this approach can be made from few tens of MeV up to about 300 MeV.

Momentum-space microscopic folding approaches for NA scattering have been extensively investigated since the mid 80s [14]. Subsequent developments led to the so called full-folding approach for the optical model potential [15,16,17,18,19,20]. Here a convolution takes place between an NN effective interaction (off-shell g- or free t-matrix, depending on the energy of application) and the ground-state nonlocal one-body mixed density of the target. Further developments within momentum-space folding approaches include the account for nuclear medium effects, as governed by genuine off-shell g matrices [21, 22,23]. An appealing feature of these approaches is that the nonlocality of the NA potential is naturally accounted for, though all those features remain undisclosed. In this work we present a means to compare them with alternative models in any representation, regardless of their local/nonlocal features. Along the process we are able to separate those Fourier components of the potential which are inherent to the NA scattering process from those that turn out irrelevant in the context of Schrödinger's wave equation.

This work is organized as follows. In sec. 2 we layout the theoretical framework and present the optical model approach to be considered as benchmark. In sec. 3 we study the effect of high momentum components of the op-

tical potential, set the threshold momentum above which scattering observables are invariant, assess the nonlocality of momentum and coordinate (local and nonlocal) potentials after ultraviolet suppression, and propose a means to assess their nonlocality. In sec. 4 we present a summary of the major findings of this work and the main conclusions. We also include an Appendix for explicit formulas used for Gaussian multipoles.

2 Framework

In the context of nucleon scattering off nuclei we express the optical model potential in momentum space as the sum of central and spin-orbit contributions

$$\tilde{U}(\boldsymbol{k}', \boldsymbol{k}; E) = \tilde{U}_c(\boldsymbol{k}', \boldsymbol{k}; E) + i\boldsymbol{\sigma} \cdot \hat{n}\, \tilde{U}_{so}(\boldsymbol{k}', \boldsymbol{k}; E)\,, \quad (1)$$

where $\frac{1}{2}\boldsymbol{\sigma}$ corresponds to the spin of the projectile and $\hat{n}$ is a unit vector perpendicular to the scattering plane, with $\boldsymbol{k}' \times \boldsymbol{k} = \hat{n}\,|\boldsymbol{k}' \times \boldsymbol{k}|$. Operator $\hat{U}$ in Eq. (1) is also denoted as $\tilde{\Sigma}(\boldsymbol{k}', \boldsymbol{k}; E)$ or $\tilde{M}(\boldsymbol{k}', \boldsymbol{k}; E)$ by other authors [24, 25].

Actual calculations of the potential in momentum space are performed over a finite mesh of relative momenta k up to some maximum value ranging from 10 up to 20 fm^{-1}, depending on the beam energy and target. Additionally, an angular mesh $\hat{k} \cdot \hat{k}'$ is designed for reliable partial wave expansion. Once the central and spin-orbit components of $\tilde{U}(\boldsymbol{k}', \boldsymbol{k}; E)$ are obtained, the corresponding partial wave components $\tilde{U}_{jl}(k', k)$ can be calculated, with j and l the total and orbital angular momenta, respectively. Detailed expressions in the context of this construction can be found in Ref. [26].

2.1 Ultraviolet suppression

Even though the optical potential is calculated in momentum space, we carry out the calculation of scattering waves and observables in coordinate space. Thus, for a given $\hat{U}(\boldsymbol{k}', \boldsymbol{k})$ we perform double Fourier Transforms (FT), which in the case of the central component of the potential takes the form

$$U_l(r', r) = \frac{2}{\pi} \int_0^\infty k'^2 dk' \int_0^\infty k^2 dk\, j_l(k'r') \tilde{U}_l(k', k) j_l(kr)\,.$$
$$(2)$$

In general this double integral results in a non-diagonal (nonlocal) function in r, r' coordinates (we omit subscript c for simplicity). Similar expressions hold for the spin-orbit term. Evaluations of the above integrals are performed up to some upper momenta chosen to ensure convergence of scattering observables. Symbolically,

$$U_l(r', r) = \frac{2}{\pi} \int_0^\infty dk' \int_0^\infty dk \cdots \rightarrow \frac{2}{\pi} \int_0^\Lambda dk' \int_0^\Lambda dk \cdots\,,$$
$$(3)$$

representing an ultraviolet cutoff of the interaction. In practice, the only condition imposed to Λ is that scattering observables remain invariant under its variations.

With this criterion set we look for the minimum Λ as function of the target mass A and the beam energy.

For the ultraviolet cutoff we use the hyperbolic regulator $f_\Lambda(k)$ defined as

$$f_\Lambda(k) = \frac{1}{2}\left[1 - \tanh\left(\frac{k-\Lambda}{\delta}\right)\right], \qquad (4)$$

which in the limit $\delta \to 0$, becomes the Heaviside step function $\Theta(\Lambda - k)$. In this study we use $\delta = 0.2$ fm^{-1}, as width of the cutoff. In what follows we focus on the implications of this cutoff, namely

$$\tilde{U}(k',k) \to \tilde{U}_\Lambda(k',k) = f_\Lambda(k')\tilde{U}(k',k)f_\Lambda(k). \qquad (5)$$

2.2 Optical-model and scattering calculations

To narrow margins of arbitrariness in the NA coupling we consider a single microscopic approach spanning over a wide energy range. To this purpose we follow Ref. [23] for momentum-space constructions, where an *in-medium NN* effective interaction is folded with the target full mixed density. The nonlocal density-dependent effective interaction is taken as the actual off-shell g matrix, solution of the Brueckner-Bethe-Goldstone equation in the Brueckner-Hartree-Fock approximation. In absence of medium effects the g matrix becomes the scattering t matrix, resulting in the impulse approximation for the optical model potential in multiple-scattering expansion [17,18,19,20,27]. The momentum-space folding approach we follow constitutes a genuine parameter-free description of nucleon scattering off nuclei at energies ranging from few tens of MeV up to 1 GeV [21,23,22].

Nuclear-matter g matrices are based on the traditional Argonne v_{18} [28] (AV18) bare potential fitted to NN phase-shift data at beam energies below pion production threshold, together with static properties of the deuteron. Additionally, we include results based on chiral effective-field-theory interaction. In this case the bare interaction is constructed with nucleons and pions as degrees of freedom, with the two-nucleon part ($2N$) fit to NN data. We use the chiral $2N$ force up to next-to-next-to-next-to-leading order (N3LO) given by Entem and Machleidt [29]. For each of these interactions we have calculated the corresponding infinite nuclear matter self-consistent single-particle fields following Refs. [30,31,32], to subsequently obtain fully off-shell g matrices.

For purposes of this study it has been crucial to rely on accurate means to obtain scattering observables in the presence of nonlocal potentials, including the long range Coulomb interaction. This is achieved with the use of recently released packages SWANLOP: Scattering WAves off NonLocal Optical Potentials [33,26]; and SIDES: Schrödinger Integro-Differential Equation Solver [34]. Both packages become suited for nucleon scattering off light and heavy targets, at beam energies ranging from a few MeV up to 1 GeV. No conditions are made to the local/nonlocal structure of the hadronic part of the potential, as long as it is finite range.

3 Calculations and findings

We begin by exploring the systematics of the resulting scattering observables under varying cutoff momenta Λ, covering a broad range of target masses A and beam energy E_{Lab}. Thus, we calculate optical model potentials for proton elastic scattering off ^{4}He, ^{16}O, ^{40}Ca, ^{90}Zr, and ^{208}Pb. Eleven beam energies are considered: 30 MeV and from 100 up to 1000 MeV in steps of 100 MeV. In this case all g matrices are based on AV18 NN bare potential. Applications for 400 MeV and above include a non-Hermitian separable term added to AV18 reference potential in order to reproduce exactly NN scattering amplitudes above pion production threshold [22]. The one-body target mixed density is represented in the Slater approximation [17], for which we only need radial point densities for protons and neutrons. In this case we use densities described in Ref. [23]. The momentum array for $\tilde{U}(k',k)$ is set as $0 \le k \le K$, with $K = \max(8$ fm$^{-1}, 2k_0)$, where k_0 is the relative momentum in the NA center-of-momentum (c.m.) reference frame.

In Fig. 1 we show the resulting total reaction cross section as function of the beam energy for proton elastic scattering off ^{4}He, ^{16}O, ^{40}Ca, ^{90}Zr, and ^{208}Pb. Gray dots denote actual results from the optical model, with dotted curves included to guide the eye. Downward red triangles denote data from Ref. [35]. Blue and green upward triangles represent data from Ref. [36], with datum for ^{208}Pb(p,p) at 860 MeV excluded as it corresponds to attenuation cross section [37,38]. We observe reasonable agreement between the calculated cross sections and the data over a broad energy range ($\sim$1 GeV), validating the physics grounds of the optical model used in this study.

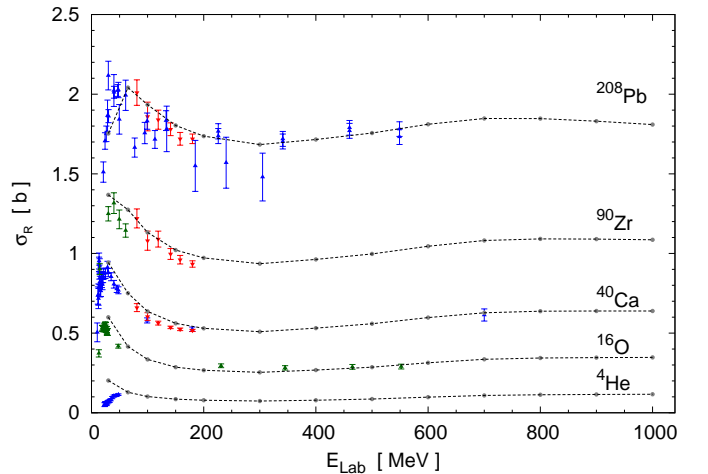**Fig. 1.** Reaction cross section for proton-nucleus elastic scattering scattering as function of the beam energy. Targets include ^{4}He, ^{16}O, ^{40}Ca, ^{90}Zr, and ^{208}Pb. Upward and downward triangles denote data from Refs. [36] and [35], respectively.

3.1 Invariant sector

We now investigate the role of high momentum components for the description of the scattering process, specifically its associated scattering observables. Thus, we look for a minimum cutoff momentum Λ which guarantees accurate results for the total reaction cross section. In Ref. [6] this study was limited to $p+^{40}$Ca scattering, obtaining that the minimum cutoff follows the rule $\Lambda^2 = \Lambda_0^2 + k_E^2$, with $\Lambda_0 = 2.4$ fm^{-1}, and k_E the momentum of the projectile in the laboratory reference frame. We aim here to extend that result by considering the cases $A = 4, 16, 40, 90,$ and 208. We proceed as follows.

For a given target and energy we calculate σ_R for a sequence of cutoff momenta Λ_i, starting from $\Lambda_1 = K$ and ending whenever Λ_i is at or below the relative momentum in the c.m. reference frame. The spacing between consecutive values of Λ is $\delta\Lambda = 0.1$ fm^{-1}. In this way the calculated reaction cross section, σ_i, will depend on the target mass number A, beam energy E and cutoff momentum Λ_i. In Fig. 2 we show the resulting reaction cross section as function of the cutoff momentum Λ. Each curve represents an specific energy. Blue curves denote results for $E = 30, 100, 200, 300$ and 400 MeV; solid black curves denote results for $E = 500$ MeV; and red curves represent results for $E = 600, 700, 800, 900$ and 1000 MeV. As observed, all cases evidence a plateau above a given cutoff momentum.
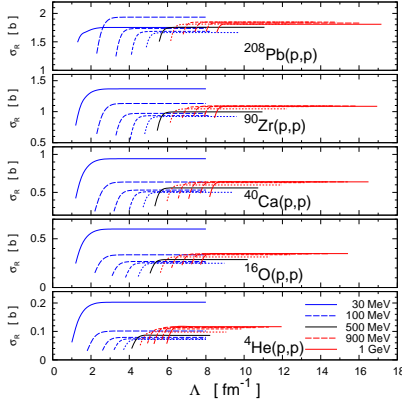

Fig. 2. Reaction cross section for proton-nucleus scattering as function of the cutoff momentum Λ applied to momentum-space optical potentials. Targets considered are ^{4}He, ^{16}O, ^{40}Ca, ^{90}Zr and ^{208}Pb, at energies between 30 MeV and 1 GeV. See text for description of curve patterns.

In order to identify the threshold cutoff momentum Q we scrutinize the cross section at the plateau. We first calculate the plateau-value cross section σ_R, which we define as the average at the plateau considering σ_i whose forward gradient $|(\sigma_{i+1} - \sigma_i)|/\delta\Lambda$, is smaller than 10^{-4} b fm. In Fig. 3 we show a logarithmic plot of the absolute difference $D_j = |\sigma(\Lambda_i) - \sigma_R|$, as function of the cutoff Λ. Curve

patterns and colors are the same as in Fig. 2. We note that the errors drop sharply with the cutoff momentum. Based on the steep descent of the error, we define the threshold cutoff momentum Q as that where the absolute error with respect to the plateau average crosses 10^{-2} b. With this criterion we obtain a well defined estimate of the minimum Λ at which the calculated cross sections does not change within the specified accuracy.
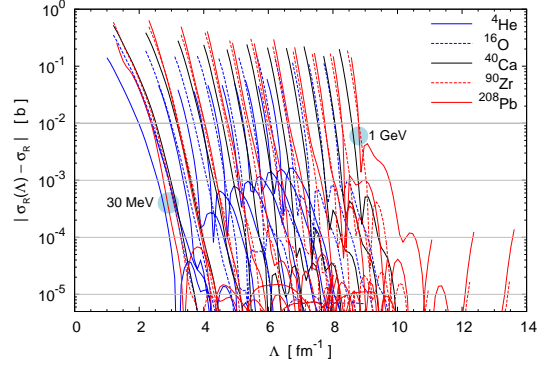

Fig. 3. Departure from the plateau-value of the calculated reaction cross section as function of Λ. Curve patterns are the same as in Fig. 2. Light-blue circles demarcate results for 30 MeV and 1 GeV, respectively.

In Fig. 4 we plot with circles the obtained threshold cutoff momentum Q as function of the beam energy E_{Lab} for the five targets under consideration. We note that the Q increases with the beam energy and the target mass number A. A simple parametrization of the observed behavior is summarized by

$$Q = \sqrt{a^2 + b\,k^2}\,, \tag{6}$$

with k the relative momentum in the NA c.m. reference frame, while a and b are parameters which depend on the target mass number A given by

$$a = \frac{3}{5}\left(4 - \frac{3}{A^{2/3}}\right)\,\text{fm}^{-1}\,; \tag{7a}$$

$$b = \frac{1.05}{1 + 1.7 \times 10^{-4}A}\,. \tag{7b}$$

Results from this parametrization are shown with solid curves in Fig. 4, where we observe a close correspondence with the calculated Q shown with circles.

It is worth stressing that the calculated Q delimits a boundary beyond which there is no meaningful physical content in the potential. This threshold is not set *a priori* but stems from a given criterion of the calculated cross sections. Any cutoff below this threshold alters the calculated observables. Conversely, whenever the cutoff is above the boundary, cross sections become invariant. This
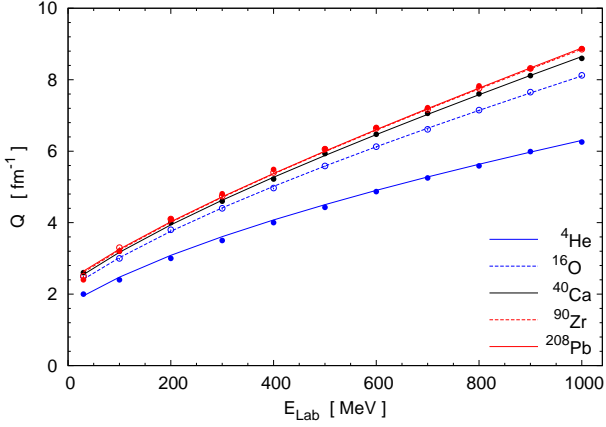
Fig. 4. Threshold cutoff momentum Q as function of beam energy for proton scattering off selected targets. Solid curves correspond to results obtained from Eq. (6).

feature is illustrated in Fig. 5, where we plot the partial contribution

$$\sigma_l = \frac{\pi}{k^2} \left[(l+1)(1 - |S_{l-1/2,l}|^2) + l(1 - |S_{l+1/2,l}|^2) \right] ,$$
(8)

as function of the orbital angular momentum l. Here $S_{jl} = \exp(2i\delta_{jl})$, with δ_{jl} the phase-shift for total and orbital angular momentum j and l, respectively. Blue, black and red curves denote results at 30 MeV, 500 MeV and 1 GeV, respectively. Labels of ^{4}He, ^{40}Ca and ^{208}Pb are shown. Solid curves correspond to results using $\Lambda = Q+1$ fm^{-1}, to move away from the transient. Dotted curves have been taken using $\Lambda = K$, the maximum momentum at which the potential has been evaluated. We observe near complete overlap between solid and dashed curves, with the exception of high l in the case of ^{40}Ca at 500 MeV, and ^{208}Pb at 1 GeV. We have found that those fluctuations are due to the exceedingly high K in both cases. The fluctuations disappear if we limit K to 12 fm^{-1}.

3.2 Momentum- and coordinate-space structure

Momentum-space potentials have the advantage of retaining naturally intrinsic nonlocalities. However, there are no studies relating their coordinate-space structure with well established models in coordinate space. Let us consider $p+^{40}$Ca elastic scattering with proton beam energy of 65 MeV. In this case we consider a momentum-space optical potential based on AV18 bare NN interaction. On the left-hand side (LHS) of Fig. 6 we show contour plots for the real (a) and imaginary (b) s-wave potential $k'\tilde{U}(k',k)k$. The corresponding coordinate-space real and imaginary parts of $r'U(r',r)r$ are shown in the right-hand side (RHS) panels (c) and (d). The momentum-space potential is calculated with $K = 8$ fm^{-1}. For clarity in the plots, the imaginary part of the potential has been multiplied by a factor of two ($\times 2$).

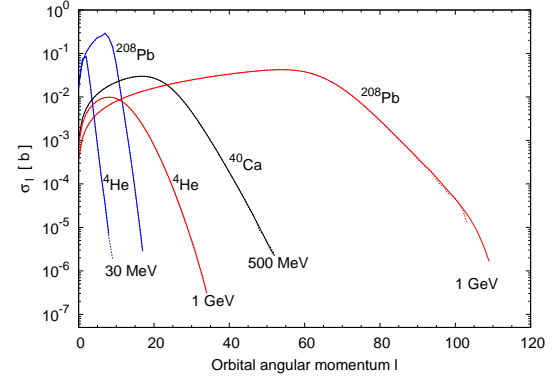We note that the momentum-space potential exhibits a smooth behavior with its dominant real and imaginary

Fig. 5. Partial absorption σ_l for proton-nucleus scattering as functions of partial waves. Blue, black and red curves denote results at 30 MeV, 500 MeV and 1 GeV, respectively. Solid curves use $\Lambda = Q+1$ fm^{-1}, from Eq. (6), while dotted curves use $\Lambda = K$.

contributions along a diagonal band, with widths of about 1.5 and 1 fm^{-1}, respectively. Their corresponding coordinate-space representation gets notoriously more structured, as evidenced in panels (c) and (d) with the sharp oscillatory patterns. The dominant terms of the coordinate-space potential also appear along the diagonal, where the deepest contributions take place.
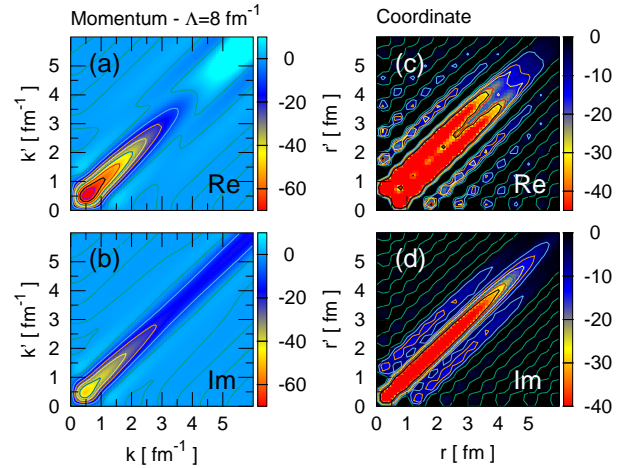

Fig. 6. s-wave optical potential based on AV18 for $p+^{40}$Ca scattering at 65 MeV. LHS (RHS) panels show potential in momentum (coordinate) representation. Upper (lower) frame show real (imaginary) part. Case for $\Lambda = 8$ fm^{-1}.

We now apply momentum cutoff to the above potential at a minimum Λ which assures to account for its associated scattering observables. To this purpose we take Q from Eq. (6), adding 1 fm^{-1} in order to move away from the transient. The resulting potentials are shown in Fig. 7, where we use the same scales and conventions as in Fig. 6.

In this case panels (a) and (b) for the momentum-space potential evidence the suppression of momentum components above Λ. As a result, its corresponding coordinate-space representation becomes less structured, with a clear and smooth distribution away from the diagonal. This extension off the diagonal in coordinate space evidences nonlocality of the interaction. Beyond the drastic differences between coordinate-space potentials shown in Figs. 6 and 7, we verify that all NA scattering observables and wavefunctions are identical within numerical accuracy.
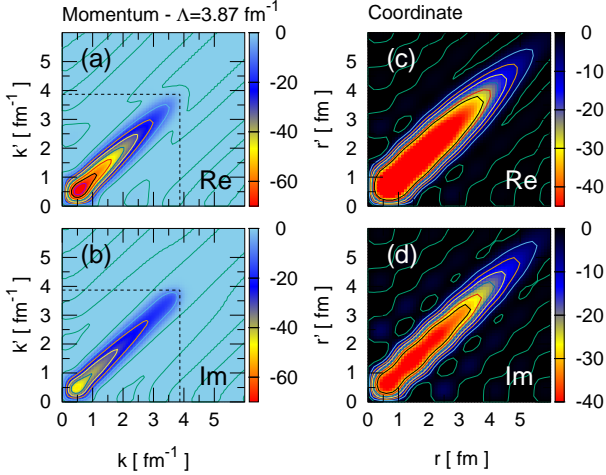

Fig. 7. The same as in Fig. 6, but with $\Lambda = 3.87$ fm^{-1}.

3.3 Assessment of nonlocality

Thus far we have only considered momentum-space potentials and their resulting coordinate-space representation after suppression of ultraviolet Fourier components. Cutoffs are applied in momentum space. We now investigate coordinate-space models. The idea in this case is to transform them into momentum space with a Fourier transform (FT), followed by a momentum cutoff at a given Λ, and transform them back to coordinate space (FT^{-1}). This procedure is illustrated in Fig. 8. For the Fourier

Fig. 8. Momentum cutoff to a potential in coordinate space.

transform back to momentum space we apply the inverse to Eq. (2), namely

$$\tilde{U}_l(k', k) = \frac{2}{\pi} \int_0^\infty r'^2 dr' \int_0^\infty r^2 dr\, j_l(k'r') U_l(r', r) j_l(kr) \, .$$
(9)

Note that this expression enables to include any kind of finite range potential, even local ones. For the latter we use $rU_l(r', r)r = V(r)\delta(r - r')$, with $\delta(r - r')$ the one-dimensional Dirac delta function and $V(r)$ the usual local potential. The suppression of the high momentum components of the local potential results in a nonlocal one.

With the above considerations we analyze Perey-Buck nonlocal potentials, using Tian-Pang-Ma (TPM) parametrization [8]. We also include in this analysis Koning-Delaroche (KD) phenomenological local optical model [7]. In this case we study $p+^{40}$Ca elastic scattering at 30.3 MeV in the laboratory reference frame. These two phenomenological potentials will be compared with microscopic momentum-space potentials based on N3LO and AV18 bare NN interactions. This energy is chosen because all four optical models are applicable. In all cases the calculated scattering observables result from momentum cutoff at $\Lambda = 3.87$ fm^{-1}, given by Eq. (6) increased by 1 fm^{-1}.

The ability of the four models to describe the data is shown in Fig. 9, where we plot the calculated differential cross section $d\sigma/d\Omega$ (a), analyzing power A_y (b) and spin rotation function Q (c) as functions of the scattering angle θ in the c.m. reference frame. The data are from Ref. [39]. The inset in (a) shows σ_l as function of the orbital angular momentum l. Results based on N3LO and AV18 potentials are denoted with black and red curves, respectively. Results for TPM parametrization and KD local potential are shown with blue solid and dashed curves, respectively. As observed, all models provide an overall reasonable description of the data, with TPM and KD in closer agreement with measurements. From this result we can state that all approaches contain the essential elements for the description of the scattering process. From the inset we also note that stronger absorption takes place for h-waves ($l = 5$), channel we shall focus attention.

In Figs. 10 we show surface plots of h-wave ($j = l + 1/2$) potentials in the rr' plane. All potentials are subject to ultraviolet cutoff $\Lambda = 3.87$ fm^{-1}. Plots (a) represent results based on N3LO, (b) for AV18, (c) for Perey-Buck nonlocal model with TMP parameters, and (d) for Koning-Delaroche (KD) local potential. The imaginary components have been amplified by three ($\times 3$) in all cases except KD, where the amplification is four times ($\times 4$). We observe that all potentials exhibit similar shapes in coordinate space, despite their different nature. Indeed, the N3LO-based optical model is constructed from chiral interactions with high momentum components already suppressed at the NN level. With this feature high Fourier components of the g matrix get suppressed, resulting in an NA potential confined in momentum space. Such is not the case of AV18, where high Fourier components are existing, extending the optical potential over the whole momentum domain. In the case of PB model, the definition of the potential in coordinate contains Fourier components over the whole spectrum, which after ultraviolet cutoff get suppressed. The same holds for KD local potential. Once transformed into momentum space and suppressed its high Fourier components, returns to coordinate space as nonlo-
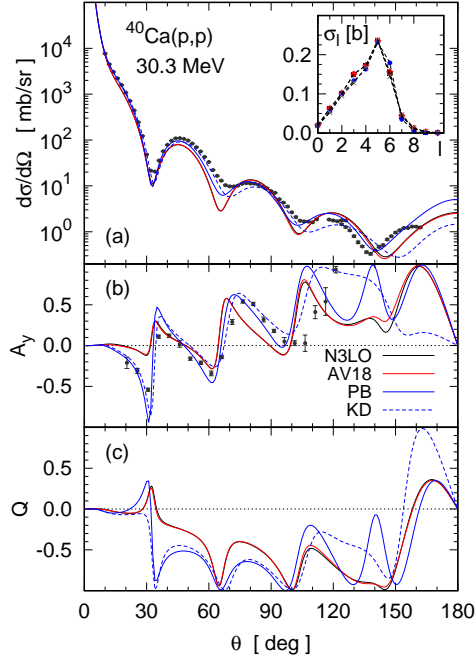
Fig. 9. Differential cross section $d\sigma/d\Omega$ (a), analyzing power A_y (b) and spin rotation function Q (c) as functions of the scattering angle θ in the c.m. reference frame. Data from Ref. [39]. See text for description of curve patterns. Inset shows σ_l as function of the orbital angular momentum l.

cal. What is remarkable in Fig. 10 is the close resemblance of the four potentials, despite their different origins.

3.4 Transversal concavity

We now pay attention to the nonlocal structure of the resulting potentials shown in Fig. 10. In particular, we focus on the transversal concavity of the potential along the diagonal. If the potential were local, then $rU(r,r')r'$ would vanish away from the diagonal $r = r'$, being very strong along the diagonal. To study these features let us introduce the alternative set coordinates xy given by

$$x = \frac{1}{\sqrt{2}}(r' + r) ; \qquad y = \frac{1}{\sqrt{2}}(r' - r) . \qquad (10)$$

As illustrated in Fig. 11, this represents a forty-five degree counter-clockwise rotation of rr' axes, with y representing the departure from the diagonal defined by $r = r'$. With these coordinates we denote $\mathcal{U}(x,y) \equiv r'U_l(r',r)r$. To examine the potential in vicinity of the diagonal we perform a series expansion up to second order in the y coordinate

$$\mathcal{U}(x,y) = \mathcal{U}(x,0) + \frac{1}{2}\mathcal{U}''(x,0)\,y^2 + \mathcal{O}(y^4) , \qquad (11)$$

with $\mathcal{U}''(x,0) \equiv \partial^2 U(x,y)/\partial y^2|_{y=0}$, the concavity of the potential on the diagonal.

To guide an interpretation of the concavity of the potential in the rr' plane, let us examine Perey-Buck nonlocal construction. In this case the central term is given the

separable structure

$$U(\boldsymbol{r}',\boldsymbol{r}) = V(\boldsymbol{R})\,H(\boldsymbol{s}) , \qquad (12)$$

where

$$\boldsymbol{R} = \tfrac{1}{2}(\boldsymbol{r} + \boldsymbol{r}') ; \qquad \boldsymbol{s} = \boldsymbol{r}' - \boldsymbol{r} . \qquad (13)$$

Form factor V is complex of Woods-Saxon type, including a surface term. The H form factor allows for nonlocality, given by a normalized Gaussian of width β expressed as

$$H(\boldsymbol{s}) = \frac{1}{\pi^{3/2}\beta^3}e^{-s^2/\beta^2} . \qquad (14)$$

Parameter β is commonly used to gauge degree of nonlocality in some studies.

To obtain the l-th multipole of the potential we evaluate

$$U_l(r',r) = 2\pi \int_{-1}^{1} P_l(u)\,V(R)\,H(s)\,du , \qquad (15)$$

where $u = \hat{r} \cdot \hat{r}'$. Since $H(s)$ is sharply peaked near $s \approx 0$, then leading contributions of V take place at $R \approx x/\sqrt{2}$. If we denote $\mathcal{U}_{PB}(x,y) = r'U_l(r',r)r$, some direct simplifications yield

$$\mathcal{U}(x,y) \approx \frac{2}{\pi^{1/2}\beta^3}V\left(\frac{x}{\sqrt{2}}\right)e^{-(x^2+y^2)/\beta^2}\,w_l\left(\frac{x^2-y^2}{\beta^2}\right) , \qquad (16)$$

where

$$w_l(b) = b\int_{-1}^{1} P_l(u)e^{bu}\,du . \qquad (17)$$

In Appendix A we provide closed expressions for $w_l(b)$ in the cases $l \leq 5$, being expressed as

$$w_l(b) = e^b y_l\left(\frac{-1}{b}\right) - e^{-b}y_l\left(\frac{1}{b}\right) , \qquad (18)$$

with $y_l(b)$ Bessel polynomials of order l. Upon substitution into Eq. (16), after Taylor expansion in the transversal coordinate y, we obtain

$$\mathcal{U}_{PB}(x,y) \approx \frac{2V(x/\sqrt{2})}{\pi^{1/2}\beta^3}\left[1 - \frac{2y^2}{\beta^2(1 - e^{-2x^2/\beta^2})} + \mathcal{O}(y^4)\right] . \qquad (19)$$

The term accompanying y^2 represents the acuteness of the potential along the diagonal, providing a quantitative measure of nonlocality. Comparing this approximate result with that in Eq. (11) lead naturally to the definition of κ, a measure of nonlocality defined as

$$\kappa = -4\frac{\mathcal{U}(x,0)}{\mathcal{U}''(x,0)} . \qquad (20)$$

In the case of approximation in Eq. (16) for PB we obtain

$$\kappa_{PB} \approx (1 - e^{-r^2/\beta^2})\,\beta^2 , \qquad (21)$$

which for $r \gg \beta$ along the diagonal converges to β^2, the square of PB nonlocality parameter. In general, κ is channel dependent.
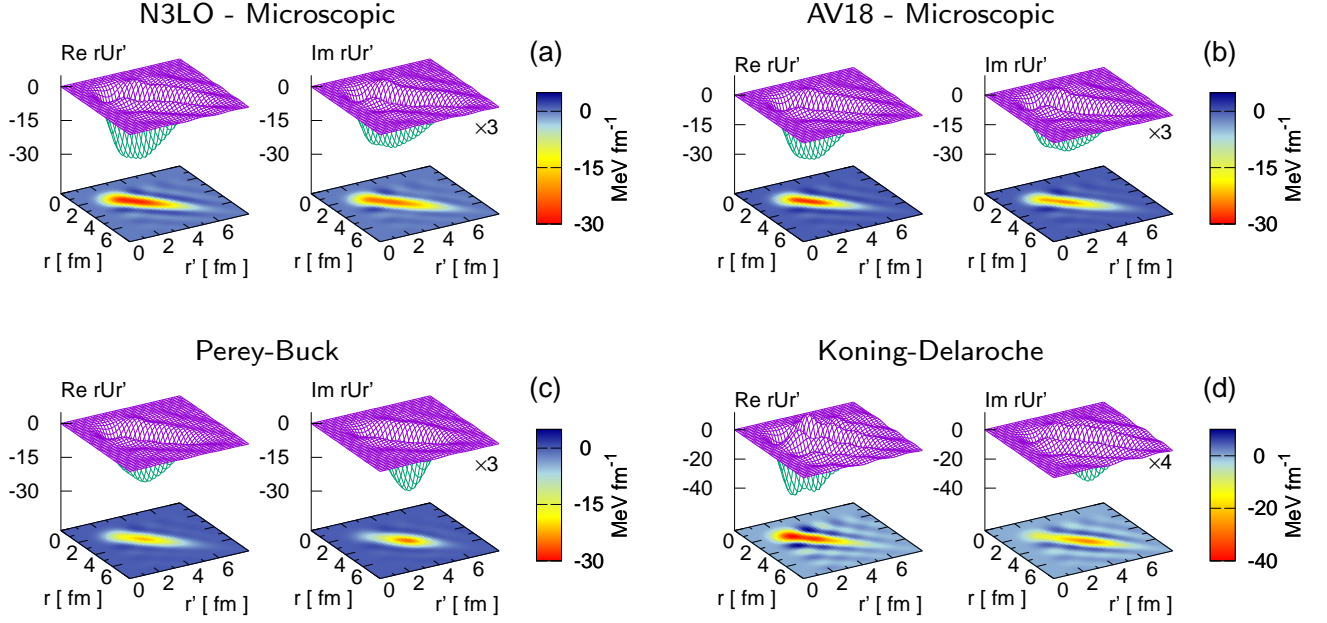
Fig. 10. Surface plots in coordinate space for h-wave ($j=5+1/2$) real (Re) and imaginary (Im) potentials. Plots (a) are for the microscopic N3LO-based potential; (b) for microscopic AV18-based potential; (c) for Perey-Buck nonlocal potential with TPM parametrization; and (d) for Koning-Delaroche local potential. All potentials have momentum cutoff at $\Lambda = 3.87$ fm^{-1}.
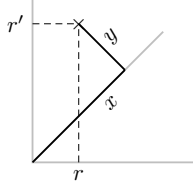

Fig. 11. Diagonal and transversal coordinates in rr' plane.

In Fig. 12 we show surface plots of s-wave potentials $rU(r,r')r'$ in the rr' plane. We include microscopic potentials based of leading-order bare potential N3LO (LHS panels) and AV18 (RHS panels). The real parts of the potentials are shown in frames (a) and (c), respectively. Their corresponding imaginary parts are shown in panels (b) and (d). Both potentials are constructed in momentum space, with $\Lambda = 12$ fm^{-1}. As in the case of h waves at 65 MeV, the coordinate-space potential is much structured and stronger in the case of AV18 than for N3LO. Observe the $[-80:80]$ MeV fm^{-1} scale in panel (c) for AV18, in contrast with $[-20:20]$ MeV fm^{-1} scale in panel (a) for N3LO.

From the above result we can now evaluate κ. In this case we treat separately the real and imaginary parts of the potential, leading to their respective κ_R and κ_I. In Fig. 13 we plot results for κ_R (solid curves) and κ_I (dashed curves) as function of r. Panels (a) and (b) show results for s and h waves, respectively. Black and red curves represent results for N3LO- and AV18-based microscopic potentials, respectively. Blue curves correspond to PB-TPM
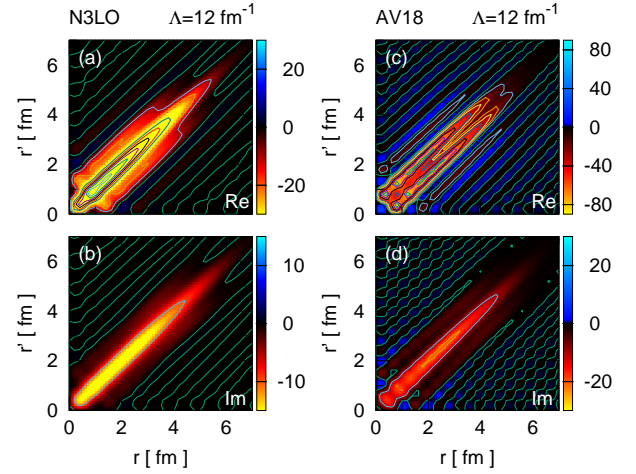

Fig. 12. Contour plots s-wave optical potential in coordinate space obtained from momentum-space calculations using N3LO (LHS panels) and AV18 (RHS panels) NN models. Momentum cutoff at $\Lambda=12$ fm^{-1}. Color bar in MeV fm^{-1} units.

nonlocal model. Dotted curves correspond to κ_{PB} as in Eq. (21). The solid light-blue line represents β^2, with $\beta = 0.88$ fm^{-1}, from TPM parametrization.

We can state the following observations: $I.-$ Black solid and dashed curves (N3LO-based) for s waves are smooth and positive, showing similar behavior for κ_R and κ_I; the same holds for h wave. The fact that these values for κ are a fraction of β^2 indicates that the potential is sharper than PB along the diagonal. $II.-$ Red solid curves (AV18-based) appear weaker than all other cases. There is also a change of sign which, after a close inspection of panel
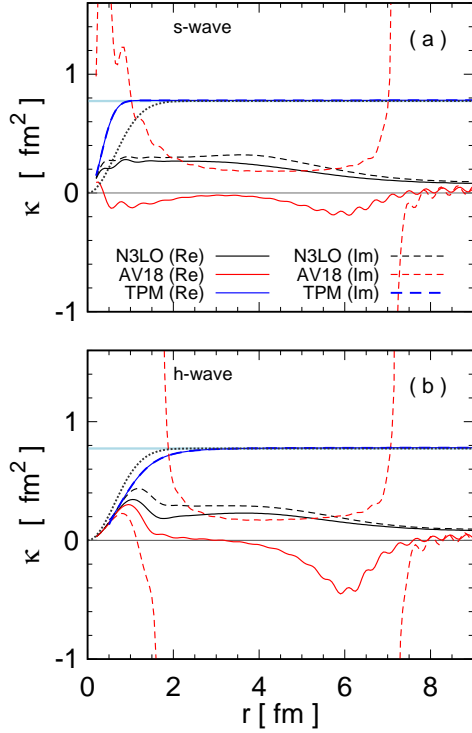
Fig. 13. Diagonal κ_R and κ_I as function of r. Panel (a) shows results for s wave, whereas panel (b) for h wave. Black and red curves correspond to N3LO- and AV18-based microscopic potentials, respectively. Blue curves correspond to PB-TPM nonlocal model. Solid and dashed curves represent κ_R and κ_I, respectively. Dotted curves correspond to approximations in Eq. (21).

Fig. 14. The same as in Fig. 12, but with $\Lambda = 3.87$ fm^{-1}.

potential as well as Koning-Delaroche local model with their momentum components above Λ suppressed. In Fig. 15 we plot κ as function of r for N3LO- and AV18-based microscopic optical potentials (black and red curves, respectively), as well as Perey-Buck nonlocal model (blue curves). Results for Koning-Delaroche potential are shown with gray curves. Solid and dashed curves correspond to κ_R and κ_I, respectively. Frames (a) and (b) show results for s and h wave, respectively. In contrast to κ in the

(c) in Fig. 12, can be attributed to change of sign of the potential. In the case of the imaginary part (red dashed curves) we observe that $\mathcal{U}''(x, 0)$ vanishes, leading to singular κ. *III.* – Solid and dashed blue curves, corresponding to PB potential, overlap completely. Additionally, they become constant for $r > 1$ fm, in the case of s waves, and for $r > 2.5$ fm, in the case of h waves. A main conclusion from the preceding analysis is that all three potentials appear quite different from one another in coordinate space. This is particularly the case of N3LO- vs AV18-based potentials, where κ_R and κ_I behave very differently. This situation changes radically with the suppression of ultraviolet components of NA potentials, as we shall see next.

Considering the same potentials as above we proceed to suppress momentum components beyond $\Lambda = Q + 1$ fm^{-1}. This is done directly to the N3LO- and AV18-based microscopic optical potentials. The resulting s-wave coordinate-space potentials are shown in Fig. 14, whose description is the same as for Fig. 12. The only difference in this case is that the color bar range in frames (a) and (c) are now the same. Observe that the suppression of high momentum components in both cases result in potentials very similar to one another.

We now examine the transversal concavity of the resulting potentials. In this analysis we include Perey-Buck
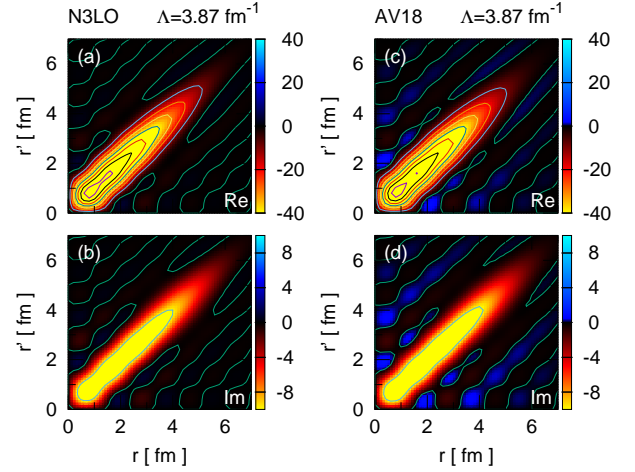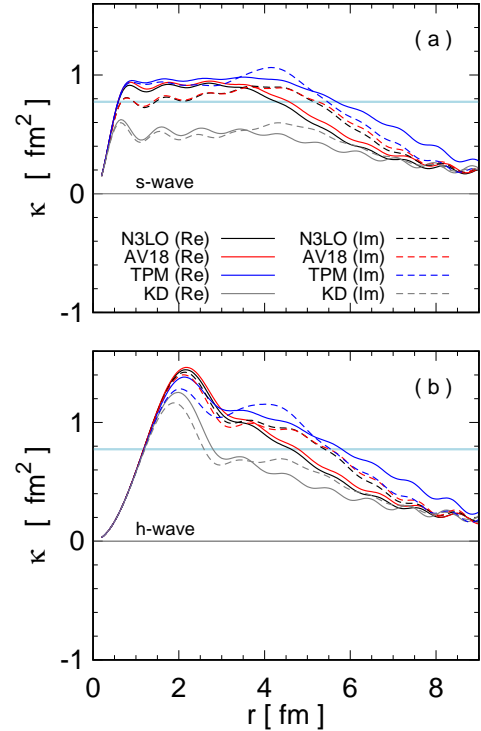

Fig. 15. The same as in Fig. 13, but with $\Lambda = 3.87$ fm^{-1}. Gray curves denote κ_R (solid) and κ_I (dashed) for KD potential.

cases with no suppression of high momentum components in the potential, results shown in Fig. 15 show smoother and less disperse behavior. Indeed, we note that N3LO- and AV18-based microscopic potentials are very similar in κ_R and κ_I, in both s and h waves. Additionally, these two models yield comparable κ in the bulk of the nucleus ($r \lesssim 3.5$ fm^{-1}). At the surface, PB model behaves more nonlocal than microscopic ones. On the other hand, when considering KD potential, the resulting nonlocality as given by κ is weaker, feature more pronounced for s waves.

3.5 Discussion

We have identified a threshold momentum Q that separates the low-momentum scale of the optical model potential from the high-momentum components. Those high momentum components become irrelevant for the evaluation of associated elastic scattering observables. We stress that the threshold momentum Q is not set *a priori* but inferred in the context of realistic constructions of optical model potentials. The criterion is that of being the smallest momentum window that enables to reproduce the scattering observables within numerical accuracy. On this regard, its philosophy differs from renormalization group techniques for the constructions of v low-k NN interactions, where a momentum cutoff is set beforehand within a coherent mathematical framework [40]. In such a case momentum-dependent NN potentials are calculated to reproduce exactly the on-shell amplitudes within a predefined momentum interval. Although in principle the scheme we have discussed here can also be extended to $A=1$, corresponding to NN scattering, such particular case would require a more focused study.

4 Summary and conclusions

We have investigated the role of high momentum components of microscopic optical model potentials for nucleon-nucleus scattering by studying its incidence on the nonlocal structure in coordinate space. The study considers closed-shell nuclei with mass number in the range $4 \leq A \leq 208$, for energies from tens of MeV up to 1 GeV. To this purpose microscopic optical model potentials are constructed in momentum space using Bruckner-Hartree-Fock g matrices based on AV18 and N3LO chiral potentials. We confirm that the gradual suppression of high-momentum contributions of the optical potential results in quite different coordinate-space counterparts, all of them accounting for the same scattering observables within an specified accuracy. Furthermore, we obtain a minimum cutoff momentum Q, function of the target mass number and energy of the process, that filters out irrelevant ultraviolet components of the potential. We also find that ultraviolet suppression to PB nonlocal potential or local Woods-Saxon potentials results in nonlocal potentials with similar appearance to microscopic models in momentum space.

With this study we have found that, for a given target and energy, there is a momentum threshold above which features of the potential become meaningless. From the prospective of momentum-space optical potential calculations, such as those investigated in Refs. [17, 18, 19, 20, 23, 27, 41], the identification of Q is particularly useful as it allows to set reliable bounds to the momentum domain over which the potential needs to be evaluated. The resulting potentials, referred as *irreducible* in Ref. [6], appear to have similar structure in coordinate space.

Optical potentials in coordinate space can be expressed in local, nonlocal or hybrid forms. Interestingly, we have found that when these potentials get suppressed their Fourier components above the threshold momentum Q, they all share similar nonlocal features. Conversely, manifest differences among local, nonlocal or hybrid potentials have as main origin the inclusion of irrelevant Fourier components. Consequently, it is safe to state that a true comparison of nonlocal features of alternative potentials for a given scattering process require the suppression of their ultraviolet components, otherwise the comparison becomes with limited scope.

A Multipoles of Gaussian form factor

We evaluate

$$w_l(b) = b \int_{-1}^{1} P_l(u) e^{bu}\, du \,, \qquad (A.1)$$

with l positive integer. For low $l \leq 3$ the evaluation of this integral is direct. For higher values they become tedious but straightforward. In such cases we use symbolic manipulation software to evaluate explicitly the cases $l \leq 5$, obtaining

$$w_0(b)/2 = \sinh b \,; \qquad\qquad (A.2a)$$
$$-b\, w_1(b)/2 = \sinh b + b \cosh b \,; \qquad (A.2b)$$
$$b^2 w_2(b)/2 = (3 + b^2) \sinh b - 3b \cosh b \,; \qquad (A.2c)$$
$$-b^3 w_3(b)/2 = (15 + b^2) \sinh b - $$
$$(15\,b + 2\,b^3) \cosh b \,; \qquad (A.2d)$$
$$b^4 w_4(b)/2 = (105 + 45\,b^2 + b^4) \sinh b - $$
$$(105\,b + 10\,b^3) \cosh b \,; \qquad (A.2e)$$
$$-b^5 w_5(b)/2 = (945 + 420\,b^2 + b^4) \sinh b - $$
$$(945\,b + 105\,b^3 + b^5) \cosh b \,. \qquad (A.2f)$$

Factorization by exponentials result in

$$w_0(b) = e^b - e^{-b} \tag{A.3a}$$

$$w_1(b) = e^b \left(1 - \frac{1}{b}\right) - e^{-b}\left(1 + \frac{1}{b}\right) \tag{A.3b}$$

$$w_2(b) = e^b \left(1 - \frac{3}{b} + \frac{3}{b^2}\right) - e^{-b}\left(1 + \frac{3}{b} + \frac{3}{b^2}\right) \tag{A.3c}$$

$$w_3(b) = e^b \left(1 - \frac{6}{b} + \frac{15}{b^2} - \frac{15}{b^3}\right) -$$
$$e^{-b}\left(1 + \frac{6}{b} + \frac{15}{b^2} + \frac{15}{b^3}\right) \tag{A.3d}$$

$$w_4(b) = e^b \left(1 - \frac{10}{b} + \frac{45}{b^2} - \frac{105}{b^3} + \frac{105}{b^4}\right) -$$
$$e^{-b}\left(1 + \frac{10}{b} + \frac{45}{b^2} + \frac{105}{b^3} + \frac{105}{b^4}\right) \tag{A.3e}$$

$$w_5(b) = e^b \left(1 - \frac{15}{b} + \frac{105}{b^2} - \frac{420}{b^3} + \frac{945}{b^4} - \frac{945}{b^5}\right) -$$
$$e^{-b}\left(1 + \frac{15}{b} + \frac{105}{b^2} + \frac{420}{b^3} + \frac{945}{b^4} + \frac{945}{b^5}\right). \tag{A.3f}$$

Here we recognize Bessel polynomials $y_n(x)$ given by

$$y_0(x) = 1 \tag{A.4a}$$
$$y_1(x) = x + 1 \tag{A.4b}$$
$$y_2(x) = 3x^2 + 3x + 1 \tag{A.4c}$$
$$y_3(x) = 15x^3 + 15x^2 + 6x + 1 \tag{A.4d}$$
$$y_4(x) = 105x^4 + 105x^3 + 45x^2 + 10x + 1 \tag{A.4e}$$
$$y_5(x) = 945x^5 + 945x^4 + 420x^3 + 105x^2 + 15x + 1 \tag{A.4f}$$

Thus,

$$w_l(b) = e^b y_l\left(\frac{-1}{b}\right) - e^{-b} y_l\left(\frac{1}{b}\right). \tag{A.5}$$

We note that Bessel polynomials are related to modified Bessel functions of the second kind through

$$y_n(x) = \sqrt{\frac{2}{\pi x}} e^{1/x} K_{n+1/2}(1/x). \tag{A.6}$$

Furthermore, they satisfy the recursion relation

$$y_{n+1}(x) = (2n+3)x\, y_n(x) + y_{n-1}(x). \tag{A.7}$$

References

1. F. Perey, B. Buck, A non-local potential model for the scattering of neutrons by nuclei, Nucl. Phys. 32 (1962) 353.

2. M. C. Atkinson, W. H. Dickhoff, M. Piarulli, A. Rios, R. B. Wiringa, Reexamining the relation between the binding energy of finite nuclei and the equation of state of infinite nuclear matter, Phys. Rev. C 102 (2020) 044333. doi:10.1103/PhysRevC.102.044333.
URL https://link.aps.org/doi/10.1103/PhysRevC.102.044333

3. C. D. Pruitt, R. J. Charity, L. G. Sobotka, J. M. Elson, D. E. M. Hoff, K. W. Brown, M. C. Atkinson, W. H. Dickhoff, H. Y. Lee, M. Devlin, N. Fotiades, S. Mosby, Isotopically resolved neutron total cross sections at intermediate energies, Phys. Rev. C 102 (2020) 034601. doi:10.1103/PhysRevC.102.034601.
URL https://link.aps.org/doi/10.1103/PhysRevC.102.034601

4. J. E. Perez Velasquez, N. G. Kelkar, N. J. Upadhyay, Assessment of nonlocal nuclear potentials in α decay, Phys. Rev. C 99 (2019) 024308. doi:10.1103/PhysRevC.99.024308.
URL https://link.aps.org/doi/10.1103/PhysRevC.99.024308

5. Y. Tian, D. Y. Pang, Z.-y. Ma, Effects of nonlocality of nuclear potentials on direct capture reactions, Phys. Rev. C 97 (2018) 064615. doi:10.1103/PhysRevC.97.064615.
URL https://link.aps.org/doi/10.1103/PhysRevC.97.064615

6. H. F. Arellano, G. Blanchon, Irreducible nonlocality of optical model potentials based on realistic nn interactions, Phys. Rev. C 98 (2018) 054616. doi:10.1103/PhysRevC.98.054616.
URL https://link.aps.org/doi/10.1103/PhysRevC.98.054616

7. A. Koning, J. Delaroche, Local and global nucleon optical models from 1 keV to 200 MeV, Nuclear Physics A 713 (3) (2003) 231 – 310. doi:https://doi.org/10.1016/S0375-9474(02)01321-0.
URL http://www.sciencedirect.com/science/article/pii/S0375947402013210

8. Y. Tian, D.-Y. Pang, Z.-Y. Ma, Systematic nonlocal optical model potential for nucleons, International Journal of Modern Physics E 24 (01) (2015) 1550006. doi:10.1142/S0218301315500068.
URL https://www.worldscientific.com/doi/abs/10.1142/S0218301315500068

9. F. A. Brieva, J. R. Rook, Nucleon-nucleus optical model potential, Nucl. Phys. A 291 (1977) 317.

10. J. P. Jeukenne, A. Lejeune, C. Mahaux, Many-body theory of nuclear matter, Phys. Rep. 25 (2) (1976) 83. doi:10.1016/0370-1573(76)90017-X.
URL http://dx.doi.org/10.1016/0370-1573(76)90017-X

11. H. V. von Geramb, The Interaction Between Medium Energy Nucleons in Nuclei, American Institute of Physics, New York, 1983.

12. K. Amos, P. J. Dortmans, H. V. von Geramb, S. Karataglidis, J. Raynal, Advances in Nuclear Physics, Vol. 25 of Advances in Nuclear Physics, Springer, New York, 2000.

13. J. Raynal, Computer code DWBA98, Tech. Rep. 1209/05, NEA (1998).

14. A. Picklesimer, P. C. Tandy, R. M. Thaler, D. H. Wolfe, Momentum space approach to microscopic effects in elastic proton scattering, Phys. Rev. C 30 (1984) 1861–1879. doi:10.1103/PhysRevC.30.1861.
URL https://link.aps.org/doi/10.1103/PhysRevC.30.1861

15. W. C. L. Ray, G.W. Hoffmann, Nonrelativistic and relativistic descriptions of proton-nucleus scattering, Physics Reports 212 (1992) 223. doi:https://doi.org/10.1016/0370-1573(92)90156-T.

URL   http://www.sciencedirect.com/science/article/pii/037015739290156T

16. H. F. Arellano, F. A. Brieva, W. G. Love, Full-folding-model description of elastic scattering at intermediate energies, Phys. Rev. Lett. 63 (1989) 605–608. doi:10.1103/PhysRevLett.63.605.
URL   https://link.aps.org/doi/10.1103/PhysRevLett.63.605

17. H. F. Arellano, F. A. Brieva, W. G. Love, Nonrelativistic full-folding model of nucleon elastic scattering at intermediate energies, Phys. Rev. C 41 (1990) 2188–2201. doi:10.1103/PhysRevC.41.2188.

18. C. Elster, T. Cheon, E. F. Redish, P. C. Tandy, Full-folding optical potentials in elastic proton-nucleus scattering, Phys. Rev. C 41 (1990) 814–827. doi:10.1103/PhysRevC.41.814.
URL   https://link.aps.org/doi/10.1103/PhysRevC.41.814

19. R. Crespo, R. C. Johnson, J. A. Tostevin, Full folding calculations for proton-nucleus elastic scattering at intermediate energies, Phys. Rev. C 41 (1990) 2257–2262. doi:10.1103/PhysRevC.41.2257.
URL   https://link.aps.org/doi/10.1103/PhysRevC.41.2257

20. M. Vorabbi, P. Finelli, C. Giusti, Theoretical optical potential derived from nucleon-nucleon chiral potentials, Phys. Rev. C 93 (2016) 034619. doi:10.1103/PhysRevC.93.034619.

21. H. F. Arellano, F. A. Brieva, W. G. Love, In-medium full-folding optical model for nucleon-nucleus elastic scattering, Phys. Rev. C 52 (1995) 301–315. doi:10.1103/PhysRevC.52.301.
URL   https://link.aps.org/doi/10.1103/PhysRevC.52.301

22. H. F. Arellano, H. V. von Geramb, Extension of the full-folding optical model for nucleon-nucleus scattering with applications up to 1.5 gev, Phys. Rev. C 66 (2002) 024602. doi:10.1103/PhysRevC.66.024602.
URL   https://link.aps.org/doi/10.1103/PhysRevC.66.024602

23. F. J. Aguayo, H. F. Arellano, Surface-peaked medium effects in the interaction of nucleons with finite nuclei, Phys. Rev. C 78 (2008) 014608. doi:10.1103/PhysRevC.78.014608.

24. J. S. Bell, E. J. Squires, A Formal Optical Model, Phys. Rev. Lett. 3 (1959) 96–97. doi:10.1103/PhysRevLett.3.96.
URL   https://link.aps.org/doi/10.1103/PhysRevLett.3.96

25. J. Rotureau, P. Danielewicz, G. Hagen, F. M. Nunes, T. Papenbrock, Optical potential from first principles, Phys. Rev. C 95 (2017) 024315. doi:10.1103/PhysRevC.95.024315.
URL   https://link.aps.org/doi/10.1103/PhysRevC.95.024315

26. H. F. Arellano, G. Blanchon, SWANLOP: Scattering waves off nonlocal optical potentials in the presence of Coulomb interactions, Computer Physics Communications 259 (2021) 107543. doi:https://doi.org/10.1016/j.cpc.2020.107543.
URL   http://www.sciencedirect.com/science/article/pii/S0010465520302599

27. S. P. Weppner, C. Elster, D. Hüber, Off-shell structures of nucleon-nucleon t matrices and their influence on nucleon-nucleus elastic scattering observables, Phys. Rev. C 57 (1998) 1378–1385. doi:10.1103/PhysRevC.57.1378.
URL   https://link.aps.org/doi/10.1103/PhysRevC.57.1378

28. R. B. Wiringa, V. G. J. Stoks, R. Schiavilla, Accurate nucleon-nucleon potential with charge-independence breaking, Phys. Rev. C 51 (1) (1995) 38–51.
URL http://link.aps.org/doi/10.1103/PhysRevC.51.38

29. D. R. Entem, R. Machleidt, Accurate charge-dependent nucleon-nucleon potential at fourth order of chiral perturbation theory, Phys. Rev. C 68 (2003) 041001. doi:10.1103/PhysRevC.68.041001.
URL http://link.aps.org/doi/10.1103/PhysRevC.68.041001

30. H. F. Arellano, J.-P. Delaroche, Low-density homogeneous symmetric nuclear matter: Disclosing dinucleons in coexisting phases, Eur. Phys. Journal A 51 (1) (2015) 7. doi:10.1140/epja/i2015-15007-2.
URL   http://link.springer.com/10.1140/epja/i2015-15007-2

31. F. Isaule, H. F. Arellano, A. Rios, Di-neutrons in neutron matter within a Brueckner-Hartree-Fock approach, Phys. Rev. C 94 (2016) 034004. doi:https://doi.org/10.1103/PhysRevC.94.034004.
URL   https://link.aps.org/doi/10.1103/PhysRevC.94.034004

32. H. F. Arellano, F. Isaule, A. Rios, Di-nucleon structures in homogeneous nuclear matter based on two- and three-nucleon interactions, Eur. Phys. Journal A 52 (9) (2016) 299. doi:https://10.1140/epja/i2016-16299-2.
URL https://doi.org/10.1140/epja/i2016-16299-2

33. H. F. Arellano, G. Blanchon, Exact scattering waves off nonlocal potentials under Coulomb interaction within Schrdinger's integro-differential equation, Physics Letters B 789 (2019) 256 – 261. doi:https://doi.org/10.1016/j.physletb.2018.12.004.
URL   http://www.sciencedirect.com/science/article/pii/S0370269318309274

34. G. Blanchon, M. Dupuis, H. F. Arellano, R. N. Bernard, B. Morillon, SIDES: Nucleon–nucleus elastic scattering code for nonlocal potential, Computer Physics Communications 254 (2020) 107340. doi:https://doi.org/10.1016/j.cpc.2020.107340.
URL   http://www.sciencedirect.com/science/article/pii/S0010465520301478

35. A. Auce, A. Ingemarsson, R. Johansson, M. Lantz, G. Tibell, R. F. Carlson, M. J. Shachno, A. A. Cowley, G. C. Hillhouse, N. M. Jacobs, J. A. Stander, J. J. v. Zyl, S. V. Förtsch, J. J. Lawrie, F. D. Smit, G. F. Steyn, Reaction cross sections for protons on ^{12}C,^{40}Ca,^{90}Zr, and ^{208}Pb at energies between 80 and 180 MeV, Phys. Rev. C 71 (2005) 064606. doi:10.1103/PhysRevC.71.064606.
URL   https://link.aps.org/doi/10.1103/PhysRevC.71.064606

36. R. Carlson, Proton-nucleus total reaction cross sections and total cross sections up to 1 GeV, Atomic Data and Nuclear Data Tables 63 (1996) 93–116. doi:https://doi.org/10.1006/adnd.1996.0010.
URL   http://www.sciencedirect.com/science/article/pii/S0092640X96900108

37. V. Lapoux, Private communication.

38. F. F. Chen, C. P. Leavitt, A. M. Shapiro, Attenuation cross sections for 860-mev protons, Phys. Rev. 99 (1955) 857–871. `doi:10.1103/PhysRev.99.857`.
URL `https://link.aps.org/doi/10.1103/PhysRev.99.857`

39. V. Hnizdo, O. Karban, J. Lowe, G. W. Greenlees, W. Makofske, Elastic Scattering of 30.3-MeV Polarized Protons from ^{40}Ca, ^{56}Fe, and ^{59}Co, Phys. Rev. C 3 (1971) 1560–1565. `doi:10.1103/PhysRevC.3.1560`.
URL `https://link.aps.org/doi/10.1103/PhysRevC.3.1560`

40. S. Bogner, R. Furnstahl, A. Schwenk, From low-momentum interactions to nuclear structure, Progress in Particle and Nuclear Physics 65 (1) (2010) 94 – 147. `doi:https://doi.org/10.1016/j.ppnp.2010.03.001`.
URL `http://www.sciencedirect.com/science/article/pii/S0146641010000347`

41. H. F. Arellano, J.-P. Delaroche, Toward an actual account for the angular dependence of the brueckner-bethe-goldstone propagator in nuclear matter, Phys. Rev. C 83 (2011) 044306. `doi:10.1103/PhysRevC.83.044306`.